

Electric control of magnetic exchange in a molecular spin triangle

Received: 22 November 2024

Accepted: 20 June 2025

Published online: 16 July 2025



Alberto Cini^{1,4}, Michael Böhme^{2,4}, Benjamin Kintzel², Mauro Perfetti³,
Winfried Plass²✉, Roberta Sessoli³✉ & Maria Fittipaldi¹✉

Spin-electric effects are crucial for quantum technologies, offering several advantages over standard magnetic field-based spin control. Seeking a mechanism independent of spin-orbit interaction, here we report the detection of a spin-electric effect in the $[\text{Cu}_3(\text{saltag})(\text{py})_6]\text{ClO}_4$ spin triangle. The effect is investigated by electron paramagnetic resonance under electric field modulation on single crystals. The anisotropy of the magnetic response to the electric field is addressed, and comprehensive ab initio calculations are performed to elucidate its origin. We demonstrate that when the electric field is applied in the plane of the triangle, the dominant contribution to the observed spin-electric signal arises from a variation of the isotropic exchange interaction. Our combined theoretical and experimental approach demonstrates that, in our system, there is no evidence of antisymmetric exchange (Dzyaloshinskii-Moriya) interaction, confirming that electric-field control of magnetic exchange is achievable in the absence of significant spin-orbit coupling. Moreover, we underscore the crucial role of the bridging ligand, which opens new avenues for chemically optimizing spin-electric coupling.

Electric control of spins is an appealing field of research in materials science^{1–6}. Its realization is expected to bring significant advantages in quantum information technology⁷, as it enables faster, less energy-consuming, and more space-confined spin manipulation compared to the use of magnetic fields. Since the electric field does not couple directly to spins, spin-electric (SE) effects based on the spin-orbit coupling (SOC) are harnessed to manipulate the spin of quantum dots⁸, diluted spins in inorganic lattices⁹, and magnetic molecules¹⁰.

A SE effect that acts directly on the exchange interactions is also very appealing because it would allow the local electric control of the interaction between spin qubits, as proposed by Kane for a scalable quantum computer¹¹. Such an effect is poorly investigated; thus, its origin and possible strategies to maximize it remain elusive. Theoretical investigations have concentrated on a simple but captivating platform: triangles of antiferromagnetically coupled half-integer spins^{12–18}. The

result of the isotropic exchange, $H_{\text{ex}} = \sum_{i=1}^3 J_{i,i+1} S_i \cdot S_{i+1}$, is the occurrence of two degenerate spin doublets if the triangle is equilateral. The attention has been concentrated on systems where SOC mediates an antisymmetric exchange interaction, also known as Dzyaloshinskii-Moriya (DM) interaction, $H_{\text{DM}} = \sum_{i=1}^3 G_{i,i+1} S_i \times S_{i+1}$. This term removes the zero-field degeneracy of the two Kramers doublets and imparts them opposite vector chirality. The resulting energy gap and the anisotropic response to the magnetic field, typical manifestations of DM interactions, are strongly affected by a lowering of the symmetry of the triangle. With the assumption that the isotropic exchange interaction is affected by the electric field, its application in the plane of the triangle lowers the symmetry and modifies the effects of DM interactions. Oscillating electric fields at the appropriate frequency can induce transitions between states of opposite chirality and the same spin projection, but also induce spin transitions for specific orientations of the magnetic field^{12,19}.

¹Department of Physics and Astronomy, University of Florence and INSTM UdR, Via Sansone 1, 50019 Sesto Fiorentino (FI), Italy. ²Institut für Anorganische und Analytische Chemie, Friedrich-Schiller-Universität Jena, Humboldtstraße 8, Jena, Germany. ³Department of Chemistry “Ugo Schiff”, University of Florence and INSTM UdR, Via della Lastruccia 3-13, 50019 Sesto Fiorentino (FI), Italy. ⁴These authors contributed equally: Alberto Cini, Michael Böhme.

✉ e-mail: sekr.plass@uni-jena.de; roberta.sessoli@unifi.it; maria.fittipaldi@unifi.it

Experimental observations of these phenomena have been recently reported for a Fe_3 triangle¹⁹ and predicted for a Cu_3 triangle²⁰. In both cases, the DM interaction is sizeable, with the ratio between the DM interaction and the isotropic coupling being (10–20)%^{21,22}. For such systems, it is difficult to distinguish the possible options for the microscopic origin of the spin-electric effect. It remains to be proven that a SE effect exists and is detectable even in the absence of DM interaction, as in the case of spin qubits, which are generally characterized by a negligible orbital contribution to maximize spin coherence.

As far as the detection of SE effects is concerned, continuous wave (CW) and pulsed electron paramagnetic resonance (EPR) spectroscopies under static electric fields have been used for decades²³. Recent experiments with electric field pulses during Hahn-echo sequences confirmed the presence of SE effects in polynuclear 3d metal complexes, such as a Cr_7Mn antiferromagnetic ring²⁴ and frustrated Cu_3 ²⁴ and Fe_3 ^{25–27} triangles. CW EPR under modulation of a moderate electric field (EFM-EPR) is an alternative technique that combines the high sensitivity of phase-sensitive detection with the possibility of investigating both diluted and concentrated samples in the single crystal form^{28–31}. The technique has been employed by some of us to study SE effects in a manganese(II)-radical molecular helix³⁰, revealing a significant modulation of the spin correlation length along the chain originated by the electric field effect on the isotropic exchange interaction.

In this work we employ an antiferromagnetic (AF) frustrated spin triangle of copper(II) $s = 1/2$ ions, selecting a molecular geometry that minimizes DM interaction, to demonstrate that a SOC-independent electric field control of the isotropic exchange can be detected at the molecular level. Non-centrosymmetric crystals of the AF copper(II) triangle³² $[\text{Cu}_3(\text{saltag})(\text{py})_6]\text{ClO}_4$ (H_5saltag = tris(2-hydroxybenzylidene)triaminoguanidine and py = pyridine), hereafter referred to as Cu_3 , previously investigated under electric field pulses in frozen solutions²⁴, are investigated by EFM-EPR spectroscopy to quantify the SE effect and characterize its anisotropy. Simulations of the EFM-EPR spectra and a comprehensive ab initio analysis of the electric field effects on different terms of the spin Hamiltonian (SH) reveal a modulation of the isotropic exchange interaction when an electric field is applied in

the plane of the triangle. No evidence of SOC-related DM interactions is detected, demonstrating that electric field control of magnetic exchange is achievable in this case as well. Interestingly, the major contribution to the SE coupling originates from the atoms of the bridging ligands, opening the perspective of tailoring it through rational chemical design.

Results

Cu_3 crystallizes in the $P31c$ non-centrosymmetric polar space group³². Each copper(II) ion is coordinated by four nitrogen and one oxygen donor. It adopts a distorted trigonal bipyramidal (tbp) geometry, with the axis of the tbp lying in the plane of the triangle. The three-fold symmetry axis at the center of the triangle relates the three copper(II) ions. The unit cell contains two crystallographically independent copper triangles (labeled **A** and **B** in Fig. 1a) and two mirror symmetry-related molecules (**A'** and **B'**) (Fig. 1b). We note that **A'** and **B** (or **A** and **B'**) are almost centrosymmetric images of each other (see Supplementary Fig. 1), making their subtle differences³² crucial for detecting the SE effect by EFM-EPR. Nevertheless, **A'** and **B** exhibit different packing along the polar c axis due to co-crystallized solvent molecules and the disordered perchlorate anions (see Supplementary Note 1).

EFM-EPR spectra

EFM-EPR experiments on a single crystal of Cu_3 were performed by replacing the magnetic field modulation (\mathbf{B}_m) of CW-EPR with a 30 kHz oscillating electric field ($\mathbf{E}_m = 69 \text{ kV m}^{-1}$). The long-wavelength \mathbf{E}_m was introduced in the comparatively small X-band cavity by means of a modified version of the standard sample-holder, consisting of a home-made propagating structure without cutoff given by two thin parallel conducting wires separated by ca. 1 mm³⁰ (a scheme of the EFM-EPR sample holder is reported in Fig. 1c and Supplementary Fig. 2). Thanks to the phase-sensitive detection, a derivative signal is revealed in the EFM-EPR spectrum if the electric field affects the resonance field, i.e., if a linear SE effect is active. Consequently, contrary to standard EPR, the absorption resonance line is modulated by \mathbf{E}_m . Moreover, the first harmonic signal cancels when responses for positive and negative \mathbf{E}_m equalize, e.g., for random distribution of orientations, along specific

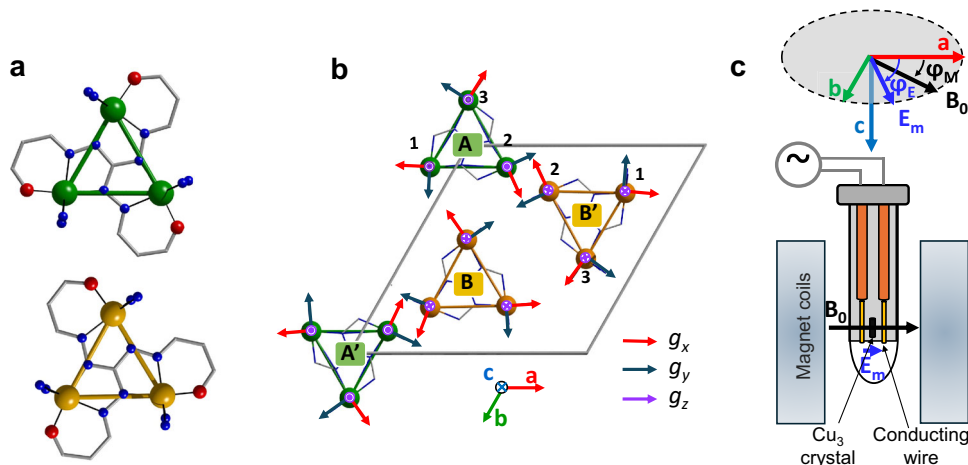


Fig. 1 | Structure, g -tensor orientation and experimental setup.

a Crystallographically independent molecules (**A**, green and **B**, orange) in the asymmetric unit of Cu_3 viewed along the crystallographic c axis (hydrogen and carbon atoms of the aromatic rings in the pyridine and Schiff-base ligands are omitted for clarity). The **A'**/**B'** families are related by pseudo-inversion symmetry with a small tilt angle of 1.2° between the triangular planes. **b** Unit cell content of Cu_3 . Triangles **A** and **A'** as well as **B** and **B'** are related by the glide reflection planes (100), (010) and (1-10), resulting in the absence of crystallographic chirality. For all

triangles, the g reference frame of the copper ions has been reported (g_x = red, g_y = blue, g_z = violet)³². Color code: Cu: green for triangles **A** and **A'** and orange for triangles **B** and **B'**; O: red, N: blue, C: grey, H and pyridine rings are omitted for clarity. Green and orange lines between the copper ions emphasize the triangular structure of the molecules. **c** Schematic representation of the sample holder for the EFM-EPR measurements and related reference frame. Images of the crystal in three experimental configurations are shown in Supplementary Fig. 2.

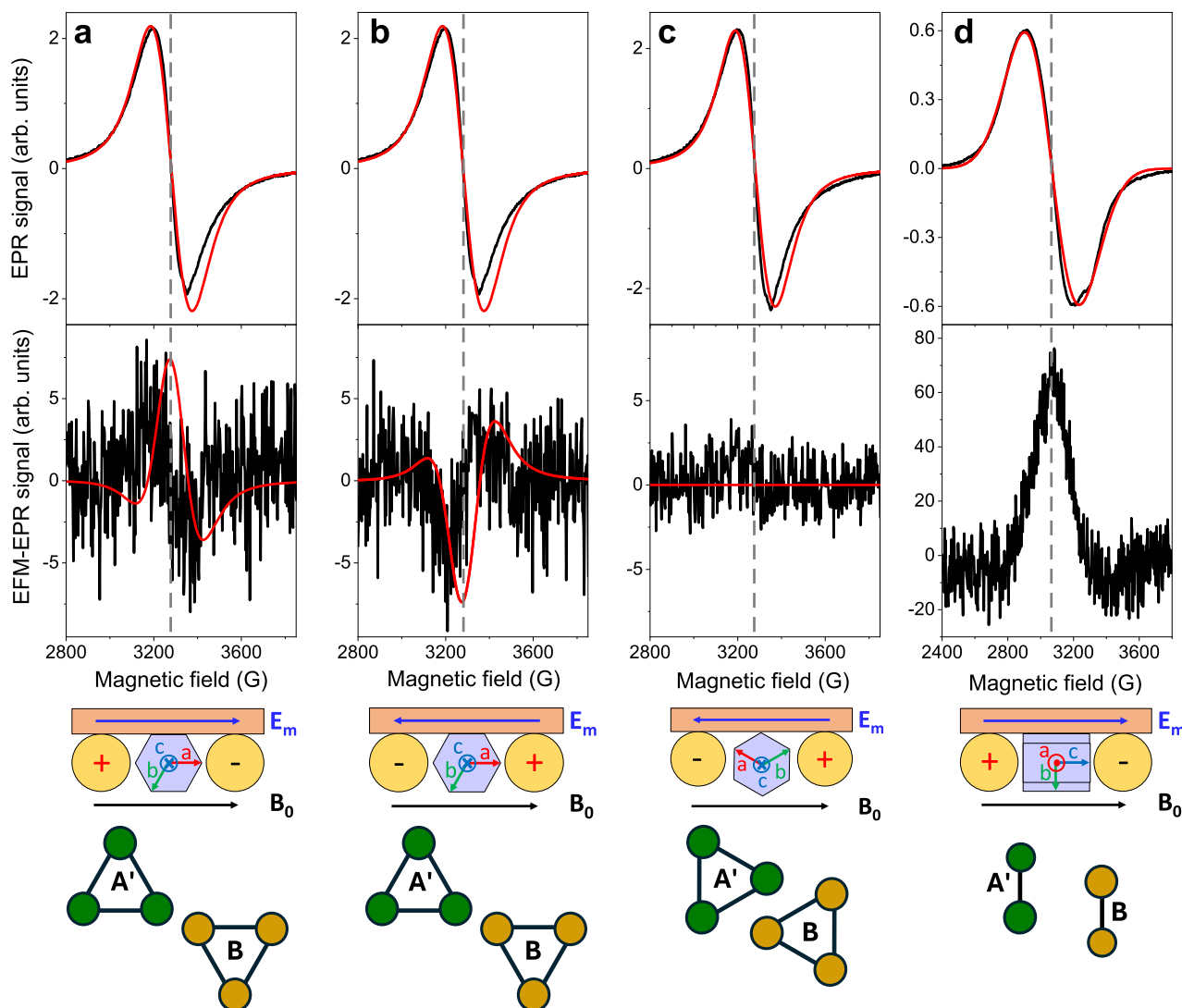


Fig. 2 | EFM-EPR spectra. EPR spectra (top panels) and corresponding EFM-EPR spectra (bottom panels) acquired on a single crystal of Cu_3 at 30 K in different experimental configurations (a schematic representation of the crystal in the sample holder for EFM-EPR viewed from the top and orientation of $\mathbf{A'}/\mathbf{B}$ triangles are reported at the bottom of the figure). For the conventional EPR spectra the \mathbf{E}_m is not present, and replaced by $\mathbf{B}_m \parallel \mathbf{B}_0$: (a) The \mathbf{a} crystallographic axis, \mathbf{B}_0 , and \mathbf{E}_m all are oriented toward the same direction ($\varphi_M = 0^\circ$, $\varphi_E = 0^\circ$); (b) The \mathbf{a} axis is parallel to \mathbf{B}_0 and antiparallel to \mathbf{E}_m ($\varphi_M = 0^\circ$, $\varphi_E = 180^\circ$); (c) A -150° rotation of the crystal about the \mathbf{c} axis and \mathbf{B}_0 parallel to $-\mathbf{E}_m$ ($\varphi_M = 150^\circ$, $\varphi_E = -30^\circ$); (d) The \mathbf{c} axis, \mathbf{B}_0 , and

\mathbf{E}_m all are oriented toward the same direction. The EFM-EPR spectra intensities are rescaled by the number of acquisitions n ($n = 15, 16, 59$, and 8 , respectively), necessary to achieve a reasonable signal-to-noise ratio. Gray dash lines indicate the EPR resonance field. In the top panels, red lines represent the simulations with the SH model given in Eq. (1) with parameters reported in Table 1. In the bottom panels, red lines represent the simulations performed using the SH model from Eq. (1) with the δg and δJ from ab initio and DFT calculations (see Table 2). Source data are provided with this paper.

symmetry directions, or when the effect is only proportional to an even power of the electric field. It is also worth noting that, although linear electric field effects can be observed in centrosymmetric crystals or frozen solutions using different techniques^{9,10,24}, provided the active site lacks an inversion center, a first-order detection by EFM-EPR requires non-centrosymmetric crystals^{23,29–31}.

The EPR and EFM-EPR spectra were acquired at 30 K for different mutual orientations between the crystal axes, the magnetic field \mathbf{B}_0 , and the electric field \mathbf{E}_m . The experimental configurations in the \mathbf{ab} plane are described in terms of the angles φ_M and φ_E , indicating the direction of the fields \mathbf{B}_0 and \mathbf{E}_m with respect to the \mathbf{a} axis, respectively (see Fig. 1c). Experimental details are reported in Methods.

The top panel of Fig. 2a shows the standard EPR spectrum with \mathbf{B}_0 in the \mathbf{ab} plane at $\varphi_M = 0^\circ$ (see Fig. 1c), which is centered at 3279 G (linewidth 160 G). The related EFM-EPR spectrum acquired with \mathbf{E}_m parallel to the \mathbf{a} axis ($\varphi_E = 0^\circ$, Fig. 2a) has the same phase and center.

Reversing the direction of \mathbf{E}_m flips the phase (Fig. 2b), and the intensity scales linearly with \mathbf{E}_m (Supplementary Fig. 3), confirming a linear SE effect. The EPR spectrum is invariant with respect to the direction of \mathbf{B}_0 in the \mathbf{ab} plane (Supplementary Fig. 4). On the contrary, when \mathbf{E}_m is applied at $\pm 30^\circ$ from the \mathbf{a} or \mathbf{b} axes, i.e., perpendicular to a glide plane, the EFM-EPR intensity drops to noise level (see Fig. 2c, Supplementary Fig. 5), matching the signal cancellation expected for $\mathbf{A'}/\mathbf{A'}$ and $\mathbf{B'}/\mathbf{B'}$ mirror-related pairs.

Finally, a broader line (320 G) is observed at ~3060 G when \mathbf{B}_0 aligns with the \mathbf{c} axis (Fig. 2d). When \mathbf{E}_m is also applied along \mathbf{c} a stronger EFM-EPR signal is observed than when \mathbf{E}_m is in the plane of the triangles. The phase changes when \mathbf{E}_m is reversed (Supplementary Fig. 6a), and the signal exhibits an absorption-like shape, differing from the \mathbf{ab} plane response. When \mathbf{E}_m is along the \mathbf{c} axis and \mathbf{B}_0 perpendicular to it, the signal shifts to high field, but the EFM-EPR line shape remains unchanged (Supplementary Fig. 6b).

Table 1 | Spin Hamiltonian parameters

Parameter	Triangle A	Triangle B
Spin	1/2	1/2
g_x	2.025	2.038
g_y	2.055	2.067
g_z	2.188	2.188
J (cm ⁻¹)	281	274
Linewidth (G) for $\mathbf{c} \perp \mathbf{B}_0$	100 (Gaussian), 120 (Lorentzian)	100 (Gaussian), 120 (Lorentzian)
H_{strain} (x, y, z) (MHz)	0, 0, 906	0, 0, 906

Values used to simulate the EPR and EFM-EPR spectra in Fig. 2: g -tensor and broadenings of the single copper ion line, and J couplings within the Cu–Cu pairs for the **A** and **B** triangles. A broadening due to a convolution of Gaussian and Lorentzian components is sufficient to reproduce the linewidth in the **ab** plane, while along **c** an H_{strain} was also used to reproduce the unresolved hyperfine splitting. The latter is less pronounced in the **ab** plane due to the smaller hyperfine couplings expected along the x and y single-ion anisotropy axes.

Spin Hamiltonian model

To simulate the EPR spectra, the spin Hamiltonian (SH) used for each C_3 symmetric triangle of the unit cell includes the Zeeman term and isotropic exchange term:

$$\hat{H} = \sum_{i=1}^3 \mu_B \mathbf{B}_0 \cdot \mathbf{g}_i \cdot \mathbf{S}_i + \sum_{ij=1i \neq j}^3 J \mathbf{S}_i \cdot \mathbf{S}_j \quad (1)$$

Ab initio calculations previously performed²³ revealed a rhombic g tensor for each copper(II) center, with slight differences between the two crystallographically independent triangles. The rhombicity of g in the spin Hamiltonian framework is related to a residual spin-orbit interaction. The smallest g value (g_x) aligns with the Cu–O bond corresponding to the axis of the tbp polyhedron oriented approximately in the **ab** plane (see Fig. 1), while the largest value (g_z) is along the **c** axis, collinear for all three ions. DFT calculations revealed strong, nearly identical isotropic antiferromagnetic coupling between the copper(II) ions for the two triangles, consistent with magnetic data³². The DM interaction was not considered as magnetic measurements suggested that $|G_{ij}/J| < 0.003$ ³². Additionally, the EPR spectra do not show the typical $g < 2$ when the magnetic field is applied in the plane, which was instead detected in Fe₃²⁵ and other Cu₃ systems with different bridging ligands^{21,22}. This assumption was validated by theoretical calculations of the energy splitting in zero field of the two ground-state Kramers doublets, ca. 0.004 cm⁻¹ (see Computational studies). The vanishing DM interaction results from the negligible overlap of the singly occupied orbital in the ground configuration of a spin site and the SOC-admixed excited state of the neighboring spin site^{21,33}. This confirms that we are exploring a different regime in Cu₃ compared to previous studies on AF triangles.

To reproduce the single-crystal EPR spectra (Fig. 2, top panels), we summed the contributions of the four molecules in the unit cell (Fig. 1b). The g values were fitted while keeping the g -principal axes and J values fixed to the computational values. The simulation parameters used are reported in Table 1, and Supplementary Note 2 contains a detailed model description. The unresolved hyperfine coupling with copper nuclear spins was neglected for the x and y components and treated as a magnetic field strain for the z direction (see Table 1). The fitting procedure for the orientational dependence of the EPR spectra is reported in Supplementary Note 3.

Simulation of the spin-electric effect: phenomenological model

The orientational dependence of the EFM-EPR spectra was phenomenologically rationalized by considering the electric field perturbation of the g -tensor and exchange coupling J in the SH described by Eq. (1). The modulated spectra were simulated as the difference between absorption spectra at $+\mathbf{E}_m$ and $-\mathbf{E}_m$ using a MATLAB script with

EasySpin³⁴ (see Methods). This approximation is valid if the shift of the resonance field is much smaller than the linewidth, as clarified by Mims²³.

Considering the SE effect as a perturbation of the g -tensor, we introduced a variation Δg_α ($\alpha = x, y, z$) for each copper(II) center:

$$g_{\alpha,E} = g_\alpha + (\hat{\alpha} \cdot \hat{\mathbf{E}}_m) \Delta g_\alpha \quad (2)$$

where $\hat{\mathbf{E}}_m$ is the unit vector of \mathbf{E}_m . The scalar product in Eq. (2) marks a simplification, as an electric field directed along the $\hat{\alpha}$ principal direction may also influence other components of the g -tensor.

According to theoretical predictions¹⁴, the effect of \mathbf{E}_m on J is proportional to the scalar product between \mathbf{E}_m and the electric dipole moment \mathbf{p}_{ij} ($ij = 12, 13, 23$; as depicted in Fig. 3a), which is associated with spins flipping from parallel to antiparallel configuration (see Computational studies), and can be expressed as follows:

$$J_{ij,E} = J + (\hat{\mathbf{E}}_m \cdot \hat{\mathbf{p}}_{ij}) \Delta J \quad (3)$$

where the unit vectors of $\hat{\mathbf{E}}_m$ and $\hat{\mathbf{p}}_{ij}$ are considered, and ΔJ is the phenomenological parameter accounting for SE coupling.

When \mathbf{E}_m is applied in the triangle plane, the J couplings increase or decrease, depending on the direction and sign of \mathbf{E}_m , lifting the degeneracy of the two ground doublets (Fig. 3b). If \mathbf{E}_m is applied along the three-fold symmetry axis, g tensors can be influenced, but any out-of-plane component of $\hat{\mathbf{p}}_{ij}$ affects all three J couplings identically, retaining the degeneracy of the two doublets. Simulated spectra for one triangle with applied \mathbf{E}_m as shown in Fig. 3a are depicted in Fig. 3c considering either a Δg or ΔJ variation. The computed angular dependence of the complete EFM-EPR signal is reported in Supplementary Fig. 7 and shows the expected 120° symmetry and the phase inversion at 60°.

This scenario remains substantially unaltered when the three-fold symmetry is removed, and two different J are assumed. Notably, the EFM-EPR detection of the variation of J induced by the electric field in the triangle requires an initial rhombicity of the g -tensor (see Supplementary Fig. 8). In extension to previous predictions¹², SOC in the case of EFM-EPR is necessary to make the individual spins distinguishable due to the different orientation of the g -tensors and to induce a resonance shift with the electric field \mathbf{E} , but it does not play any role in the SE coupling. The phenomenological model qualitatively describes the SE effect for an individual triangle; if all triangles were symmetry-related, a quantitative estimation of a linear SE effect would be possible by comparing the rescaled EFM-EPR and EPR intensities³⁰. However, the EFM-EPR signals of the two families in the unit cell must be considered (Supplementary Figs. 9, 10 and Supplementary Note 4). The result is that for Cu₃ crystals, the EFM-EPR signal is much weaker than the contributions of the individual triangles due to cancellation by superposition and is highly sensitive to subtle SH parameter differences between the two sets of pseudo-inversion symmetry-related triangles, preventing direct SE parameter quantification. To resolve this issue and separate the contributions to the SE effect, we performed ab initio computational studies.

Computational studies

An electric field affects a spin system through both electronic and ionic components, originating from electron density deformation and atomic displacement, respectively^{35,36}. Computational studies for the exchange-coupled triangular complex Cu₃ allow us to disentangle these contributions and quantify their impact on the g -tensor $\delta g(\mathbf{E}_m)$ and coupling constants $\delta J(\mathbf{E}_m)$.

The prerequisite for SE coupling is the presence of electric dipole moments in the spin-frustrated ground state of the Cu₃ molecule, which were investigated using the broken-symmetry (BS)-DFT ansatz. After calculating the high-spin (HS) state ($|\uparrow\uparrow\uparrow\rangle$), a spin-flip procedure

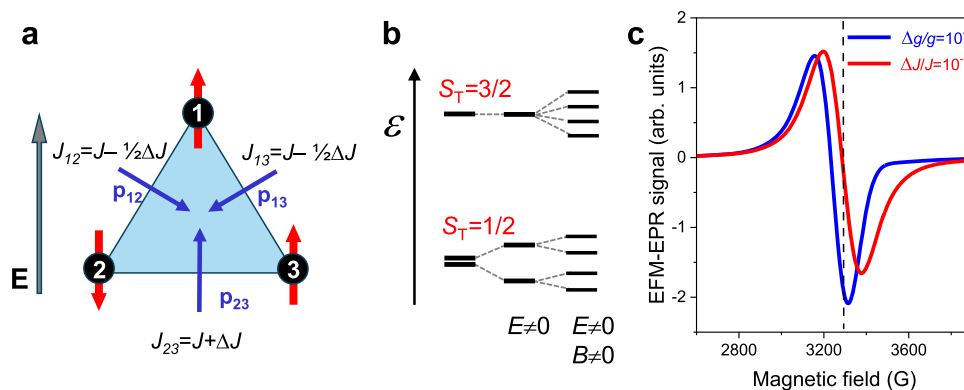


Fig. 3 | Schematic representation of the spin-electric effect inside a spin-frustrated triangle. **a** Effect of an electric field \mathbf{E} applied in the plane of the triangle on the exchange coupling constant of each Cu–Cu pair, with the simplifying assumption of the relevant dipole moment being perpendicular to the Cu–Cu direction and pointing towards the center of the triangle, i.e., assuming a D_{3h} symmetry for the system, which does not alter the ground-state characteristics in terms of chirality compared to the real C_3 molecular symmetry of Cu_3 . **b** Energy levels of the spin triangle showing the two ground-state Kramers doublets¹⁵. If only isotropic exchange is active, the two doublets are degenerate and the eigenvalue of the spin chirality operator is zero. In the absence of DM, the degeneracy can be lifted by applying an in-plane electric field \mathbf{E} or by simultaneously applying an additional magnetic field \mathbf{B} , as illustrated. **c**, EFM-EPR spectra for a single triangle (**A**) with \mathbf{E}_m and \mathbf{B}_0 in the plane of the triangle and perpendicular to one Cu–A vector, simulated by using the SH parameters reported in Table 1, and different SE mechanisms. The blue line is computed assuming that the electric field induces $\Delta g_\alpha/g_\alpha = \Delta g_\beta/g_\beta = 10^{-6}$ for each Cu ion according to Eq. (2), while the red line is obtained assuming a variation $\Delta J/J = 10^{-5}$ for each Cu pair according to Eq. (3). The dashed black line shows the center of the EPR spectrum of the triangle.

was applied to break the wavefunction symmetry. The charge rearrangement in the BS state and the resulting in-plane dipole moment \mathbf{p}_{xy} ($|\mathbf{p}_{xy}| = \sqrt{p_x^2 + p_y^2} = 2.61 \times 10^{-31}/2.55 \times 10^{-31}$ C m for \mathbf{A}'/\mathbf{B}) are shown in Fig. 4. As each BS state represents only one possible spin configuration, whereas each doublet of the spin-frustrated ground state consists of an equally weighted linear combination of all three configurations ($|\uparrow\downarrow\uparrow\rangle$, $|\uparrow\uparrow\downarrow\rangle$, and $|\uparrow\downarrow\downarrow\rangle$), there is no permanent dipole in the \mathbf{ab} plane. However, the application of an external electric field unbalances the energy and weight of the three BS configurations, resulting in the EFM-EPR signal. In a chemical picture, the SE effect originates from the presence of an in-plane C_3 -symmetric radial charge disparity in the electronic ground state of the spin-frustrated triangular molecule. In contrast, the C_3 symmetry allows a permanent dipole moment \mathbf{p}_z along \mathbf{c} in the BS state ($|\mathbf{p}_z|$ for \mathbf{A}'/\mathbf{B} : $1.07 \times 10^{-30}/1.25 \times 10^{-30}$ C m), with a similar value for the HS state, which is about five times larger than the in-plane moment \mathbf{p}_{xy} .

In Fig. 4, it is apparent that after flipping the spin of Cu1 ($|\uparrow\uparrow\uparrow\rangle \rightarrow |\downarrow\uparrow\uparrow\rangle$), the orientation of the dipole moment \mathbf{p}_{xy} does not fully coincide with the position vector of the flipped spin center, as schematized in Fig. 3. This is related to the lower C_3 symmetry and can be rationalized by the electron density of the bridging diazine moiety, which is asymmetric with respect to Cu–Cu vectors (Supplementary Fig. 11). Separation of \mathbf{p}_{xy} into a metal ($\mathbf{p}_{xy}^{\text{Cu}}$) and ligand part ($\mathbf{p}_{xy}^{\text{L}}$), are depicted in Fig. 4 and their calculation is discussed in Supplementary Note 5. As expected, the more pronounced changes in electron density upon spin-flipping are localized on the copper sites. However, having both negative and positive signs, they weakly impact the induced dipole moment. On the contrary, the atoms on the bridging ligands exhibit clear electron depletion on the salt arms bound to the flipped spin, thus providing the leading contribution to \mathbf{p}_{xy} . This suggests that ligand modifications influencing the radial charge disparity could eventually allow tuning the SE effect. Indeed, the computed \mathbf{p}_{xy} are around two orders of magnitude larger than the one computed for a Cu_3 polyoxometalate structure¹⁴.

The electric field dependence $\delta J_{ij}(\mathbf{E}_m)$ of the individual magnetic Cu–Cu pair interactions required for the EFM-EPR simulation were computed using electric-field-dependent broken-symmetry (EFD-BS) DFT (Supplementary Note 6). Under experimental conditions (69 kV m^{-1} , the largest $|\delta J|$ was calculated to be $6.0 \times 10^{-4} \text{ cm}^{-1}$ (**A'**) and $5.9 \times 10^{-4} \text{ cm}^{-1}$ (**B**) (Table 2 and Supplementary Note 6), yielding

relative magnitudes of $|\delta J/J| = 2.14 \times 10^{-6}$ and 2.15×10^{-6} for the two triangles, respectively. The quadratic Stark effect, depending on the polarizability, was found negligible for the applied experimental field (Supplementary Note 6).

While DFT methods are known to provide accurate estimates of magnetic exchange interactions at an affordable computation cost, more demanding ab initio CASSCF/RASSI-SO calculations in the presence of electric fields were necessary to compute the SE effect on the local g -tensor of the individual copper ions, denoted as $\delta g(\mathbf{E}_m)$ (Supplementary Note 7). The influence of the electric-field components E_k ($k = \{X, Y, Z\}$), expressed in the orthogonal crystal reference frame (\mathbf{abc}), on the single-ion g -tensor can be quantified by the SE coupling-tensor components $T_k = \frac{\partial g}{\partial E_k}$ within the frame of the local magnetic axes ($\alpha = \{x, y, z\}$). Due to the low local symmetry, all T_k are non-zero, indicating a strong anisotropy (Supplementary Note 7). Notably, $T_k(\mathbf{A}) \approx -T_k(\mathbf{B})$ are consistent with the pseudo-inversion center. The largest in-plane absolute tensor component is $|T_{xy}| = 1.8 \times 10^{-12} \text{ m V}^{-1}$ (**A'**) and $1.6 \times 10^{-12} \text{ m V}^{-1}$ (**B**), leading to a $|\delta g|$ of approximately 1.2×10^{-7} (**A'**) and 1.1×10^{-7} (**B**) under the experimentally applied electric field. The relative effect $|\delta g/g|$ is $\sim 6 \times 10^{-8}$, significantly smaller than $|\delta J/J|$. $|\mathbf{p}_{xy}^{\text{Cu}}| < |\mathbf{p}_{xy}^{\text{L}}|$.

The permanent \mathbf{p}_z dipole allows for atomic displacement under an electric field^{35,36}. To investigate the extent of the phenomenon and its effect on SH parameters, DFT geometry optimizations under applied electric fields along the \mathbf{c} axis and subsequent ab initio CASSCF/RASSI-SO calculations were performed (Supplementary Note 8). The resulting effect, represented by $\delta g^{\text{disp}}(\mathbf{E}_m)$, is shown in Table 2. Clearly, along \mathbf{c} the atomic displacement dominates over the effect on the electronic cloud, being one order of magnitude larger (largest $|\delta g^{\text{disp}}|$ at 69 kV m^{-1} : 6.0×10^{-6} (**A'**), 5.2×10^{-6} (**B**)). Furthermore, this effect strongly depends on the modeling of the disorder in the perchlorate anions near the trinuclear cationic complexes.

Simulation of the EFM-EPR spectra

The ab initio calculated field-dependent quantities $\delta g(\mathbf{E}_m)$, $\delta g^{\text{disp}}(\mathbf{E}_m)$, and $\delta J(\mathbf{E}_m)$ were used to simulate the EFM-EPR spectra (Supplementary Note 9).

Concerning the effect on the g -tensor, Eq. (2) was modified ($\Delta g_\alpha \rightarrow \delta g_\alpha(\mathbf{E}_m)$) according to the calculated T_{ij} matrix elements (Supplementary Note 7) as in Eq. (4), which also includes the deformation

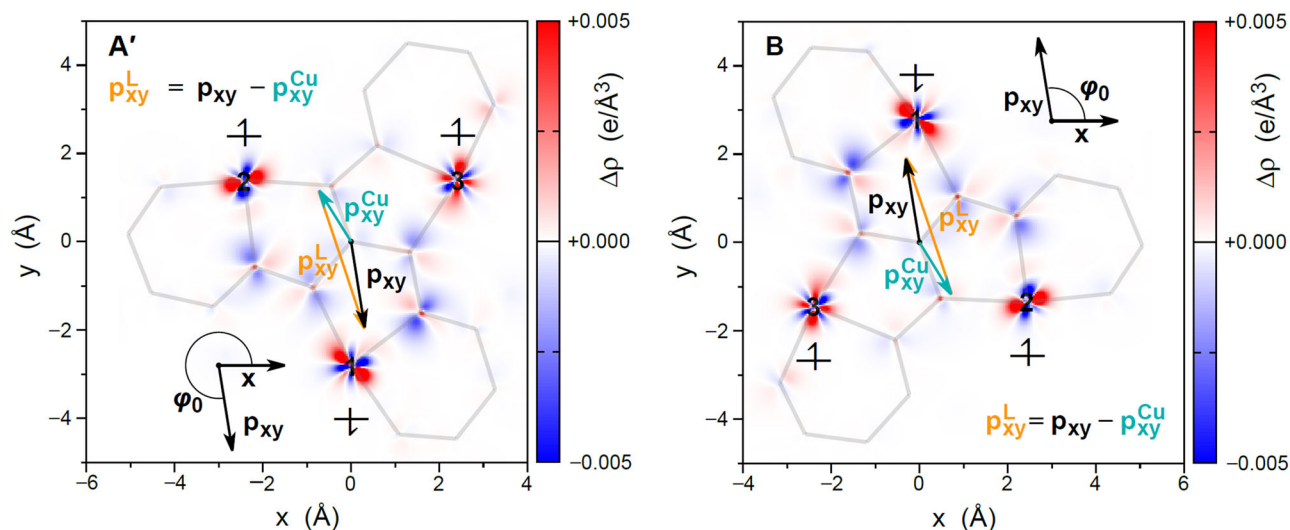


Fig. 4 | Ab initio calculated charge distribution. Contour plots representing the computed change in charge density within the trinuclear copper plane for the molecular species **A'** (left) and **B** (right) in Cu_3 after flipping the spin of Cu1 ($\downarrow\uparrow\uparrow$), starting from the C_3 symmetric ferromagnetic state ($\uparrow\uparrow\uparrow$). Grey lines represent chelate rings in the molecular structures. The in-plane dipole moment \mathbf{p}_{xy} is shown as a black arrow. The insets define the angle ϕ_0 between the x -axis and \mathbf{p}_{xy} , where x corresponds to the Cu2-Cu3 direction. The dipole moment $\mathbf{p}_{xy}^{\text{Cu}}$ (cyan vector) of the three copper centers was obtained by a charge separation procedure utilizing natural atomic orbitals (see Supplementary Note 5). The dipole moment $\mathbf{p}_{xy}^{\text{L}}$ (orange vector) corresponding to the ligand system was determined by the difference $\mathbf{p}_{xy}^{\text{L}} = \mathbf{p}_{xy} - \mathbf{p}_{xy}^{\text{Cu}}$.

effect along the z axis, represented by \mathbf{T}^{disp} . Note that all three g_α values are affected by a general orientation of the electric field.

$$g_\alpha(\mathbf{E}_m) = g_\alpha + \delta g_\alpha(\mathbf{E}_m) \text{ with } \delta g(\mathbf{E}_m) = (\mathbf{T} + \mathbf{T}^{\text{disp}}) \cdot \mathbf{E}_m \quad (4)$$

The effect on the exchange constant of each Cu–Cu pair was adapted from Eq. (3) ($\Delta J_{ij} \rightarrow \delta J_{ij}(\mathbf{E}_m)$) to incorporate EFD-BS-DFT results, leading to Eq. (5).

$$J_{ij}(\mathbf{E}_m) = J + \delta J_{ij}(\mathbf{E}_m) \quad (5)$$

The modulation of exchange constants by the electric field (δJ_{12} , δJ_{13} , and δJ_{23}) for each copper triangle is given in Supplementary Note 6, considering the dipole moment orientations.

Using the ab initio calculated parameters, the intensity of the single-crystal EFM-EPR spectra in the **ab** plane is correctly simulated, while the shape, as well as the center of the spectrum, are only approximately reproduced (Fig. 2a–c). Despite that, it is evident that for in-plane EFM-EPR spectra the effect induced by $\delta J(\mathbf{E}_m)$ dominates over the one induced by $\delta g(\mathbf{E}_m)$ (Supplementary Figs. 12 and 13), as $|\delta J/J|$ is about 35 times larger than $|\delta g/g|$. Moreover, the comparison of the simulated EFM-EPR signals between individual triangles and the crystal unit cell shows that, in the **ab** plane, only ca. 25% of the signal of the individual triangles is left due to the partial cancellation resulting from pseudo-inversion symmetry between the two families of molecules (Supplementary Fig. 14).

When electric and magnetic fields are oriented along the polar c axis, atomic displacements by the electric field due to the permanent dipole moment \mathbf{p}_z become dominant. The best agreement with experimental data was found with one perchlorate species per trinuclear complex (Supplementary Note 8). The distinct shape of the EFM-EPR signal compared to that in the **ab** plane is attributed to the vanishing $|\delta g_z^{\text{disp}}|$, resulting in no shift of the individual signals. Simultaneously, the larger in-plane $|\delta g_{x,y}^{\text{disp}}|$ values alter transition probabilities and EPR intensity, resulting in the absorption-like EFM-EPR signal, in contrast to the first derivative shape of the weaker purely electronic $\delta g(\mathbf{E}_m)$ contribution (Supplementary Fig. 15). Including both $\delta g(\mathbf{E}_m)$ and $\delta g^{\text{disp}}(\mathbf{E}_m)$ effects, the simulated spectrum reproduces the experimental shape but with lower intensity (Supplementary Fig. 16). This discrepancy could arise from approximations in the theoretical

Table 2 | Calculated SE coupling parameters

Triangle		$ \delta J $		
$\mathbf{E}_m \parallel \mathbf{p}_{xy}$	A'	$6.0 \times 10^{-4} \text{ cm}^{-1}$		
	B	$5.9 \times 10^{-4} \text{ cm}^{-1}$		
		$\delta g_x \times 10^{-7}$	$\delta g_y \times 10^{-7}$	$\delta g_z \times 10^{-7}$
$\mathbf{E}_m \parallel \mathbf{a}$	A'	0.3	−1.2	−0.1
	B	−0.3	1.1	0.2
$\mathbf{E}_m \parallel \mathbf{c}$	A'	−0.3	1.5	−0.7
	B	0.4	−1.7	0.8
		$\delta g_x^{\text{disp}} \times 10^{-7}$	$\delta g_y^{\text{disp}} \times 10^{-7}$	$\delta g_z^{\text{disp}} \times 10^{-7}$
$\mathbf{E}_m \parallel \mathbf{c}$	A'	−20.3	60.0	0.0
	B	17.5	−52.1	0.0

Values refer to copper ion Cu1 of the triangles **A'** and **B**. $|\delta J|$ induced by the electric field based on EFD-BS-DFT calculations for \mathbf{E}_m of 69 kV m^{-1} and parallel to the corresponding \mathbf{p}_{xy} . δg_α derived from the calculated SE coupling tensor components T_k as determined by ab initio calculations for \mathbf{E}_m of 69 kV m^{-1} and parallel to the crystallographic **a** and **c** axes. $\delta g_\alpha^{\text{disp}}$ derived from geometry optimizations at DFT level of theory under applied electric fields and subsequent ab initio calculations for \mathbf{E}_m of 69 kV m^{-1} and parallel to the crystallographic **c** axis.

calculation and/or unresolved hyperfine interactions with the copper nuclear spin. Generally, hyperfine interactions in metal ions correlate with g values and are expected to be affected by electric fields^{37,38} (Supplementary Note 9). A tentative simulation addressing the implications of electric field effects on unresolved copper hyperfine interactions is reported in Supplementary Fig. 16.

Discussion

Frustrated AF spin triangles are a fascinating workbench to explore the electric field control of spin systems. Studies on Cu_3 in frozen solution indicated SE coupling via pulsed EPR due to its good spin coherence²⁴. However, single-crystal investigations are superior for detecting anisotropy of interactions, which is fundamental to discriminating its microscopic origin. For Cu_3 , where a diamagnetic isostructural crystalline host for echo-detected experiments is lacking, CW EFM-EPR spectroscopy is key to accessing SE phenomena.

Detailed analysis of EFM-EPR spectra, supported by *ab initio* computational studies, allowed rationalizing the large anisotropy of the SE effect, revealing that perpendicular to the triangular plane atomic displacement - driven by a permanent electric dipole moment - dominates the SE effect on the *g*-tensors, being two orders of magnitude larger than the influence on the electronic cloud. In contrast, when the \mathbf{E}_m field is applied within the triangular plane, where a permanent electric dipole moment is absent, only the latter effect is permitted. The resulting SOC-independent modulation of the isotropic exchange interaction ($\Delta J \sim 10^{-3} \text{ cm}^{-1}$, or $10^{-8} \text{ cm}^{-1}/(\text{Vm}^{-1})$) leads to satisfactory simulation of the experimental EFM-EPR spectra and is the leading term in the SE coupling, overcoming the effect on the *g*-tensors mediated by the residual SOC.

The modulation in *J*, originating from the in-plane dipole moment of the spin-frustrated ground state, is dominated by ligand contributions, highlighting the major influence of the electric field on the electronic cloud of the ligand. Interestingly, the electric field effect on *J* appears to be significantly larger than that computed for a polyoxometalate Cu_3 system¹⁴ but about two orders of magnitude smaller than that observed in a Mn-radical helix³⁰, where the bridging ligand carries an unpaired electron in a largely delocalized molecular orbital. Our findings pave the way for a rational design of bridging ligands, unlocking enhanced control over spin-spin exchange interaction with electric fields. This novel SE mechanism of exchange control, independent of spin-orbit contributions and atomic displacement, could be a key factor in implementing scalable architectures for quantum information based on molecular spin qubits.

Methods

Sample preparation

Single crystals of $[\text{Cu}_3(\text{saltag}(\text{py})_6)\text{ClO}_4]$ with the shape of hexagonal rods and dimensions of approximately $1 \text{ mm} \times 1 \text{ mm} \times 2 \text{ mm}$ were obtained by a modified procedure from bulk material synthesized following the procedure reported by some of us³².

EPR and EFM-EPR measurements

X-band EPR measurements were performed using a 9 GHz Elexys E500 instrument (Bruker) equipped with a microwave frequency counter. An Oxford Instruments ESR900 continuous He flow cryostat was used to achieve low temperatures. An ER4122SHQE EPR resonator (Bruker) was used for the measurements.

The single-crystal EPR study of Cu_3 was realized at 20 K (see Supplementary Note 3). The EFM-EPR and the corresponding EPR spectra of Fig. 2 were acquired at 30 K, where optimal temperature stability in the presence of the heat load of the EFM-EPR setup is guaranteed. EPR spectra were acquired with a magnetic field modulation amplitude of 5 G, frequency of 100 kHz and a microwave power of $53 \mu\text{W}$. The magnetic field sweeps of 1670 G in the *ab* plane and 1400 G along *c* were sampled with 2048 points, a time constant of 40.96 ms, and a conversion time of 20.48 ms, resulting in an acquisition time of 42 s for each spectrum. Details on the fitting procedure of the single-crystal EPR spectra and data evaluation can be found in Supplementary Note 3. EFM-EPR measurements were realized with the same setup as used for the EPR measurements, except for the modified version of the sample holder (see Fig. 1c, already described in ref. 30). A 30 kHz oscillating electric field of the order of 69 kV m^{-1} was used. The applied voltage was taken from the external modulation output of the EPR console, the signal passed through a home-made electronic circuit for a 180° phase control, and subsequently amplified using a high-voltage amplifier (Trek, model 50/750). Therefore, a voltage of about 76 V was fed into the wires, the distance of which was around 1.1 mm. To avoid discharge, the EPR tube hosting the electrodes and the sample was filled with He gas and sealed. The EFM-EPR spectra were acquired with 1000 times higher microwave power with respect to the EPR spectra. The magnetic field sweep of 1400 G was sampled with 512

points, a time constant of 327.68 ms, and a conversion time of 1310.72 ms, resulting in an acquisition time of 671 s. Moreover, multiple acquisitions were needed to increase the signal-to-noise ratio of EFM-EPR spectra. The number of acquisitions varied in the range 10 – 60, depending on the intensity and shape of the EFM-EPR signal. Given the low intensity of the detected EFM-EPR spectra, the system was left to thermally equilibrate for two hours to warrant the necessary thermal stability before the measurements. The reported signals (Fig. 2, bottom panels) are the sum of all the acquisitions normalized to the number of acquisitions.

Different experimental configurations were realized by inverting the sign of \mathbf{E}_m and by rotating the sample holder about its vertical axis to vary the relative orientation between \mathbf{E}_m and the static magnetic field \mathbf{B}_0 , and by mounting the crystal in different orientations. Moreover, the anisotropy of the SE effect in the crystallographic *ab* plane was investigated by rotating the crystal about its *c* axis every 30° .

Computational details

Structures for the computational models **A'** and **B** were taken from the original publication of Cu_3 ³². All DFT calculations have been performed with the Turbomole v7.2 package of programs³⁹, utilizing def2-TZVPP basis sets⁴⁰. To obtain high precision results, a fine DFT grid (grid 7) combined with a high SCF convergence threshold of 10^{-10} Hartree was used for all DFT calculations. The procedure for separating the dipole moment contributions based on a natural population analysis and corresponding natural atomic orbitals⁴¹ is described in Supplementary Note 5. Computational results from the initial publication of Cu_3 ³², namely the high-spin (HS) and broken-symmetry (BS) state calculations for **A'** and **B**, respectively, were used as a base for the theoretical studies in this work to obtain the electric-field dependence $\delta J_{ij}(\mathbf{E}_m)$ in the individual coupling constants (see Supplementary Note 6 for further details). *Ab initio* calculations (CASSCF/RASSI-SO) were performed with the OpenMolcas v18.09 package of programs⁴² based on different computational model structures (for more details see Supplementary Note 7). State-averaged CASSCF calculations were performed for the ^2D multiplet (5 states) with an active space consisting of 9 electrons in 5 orbitals which represented the $3d^9$ valence shell of a copper(II) ion. For all *ab initio* calculations, the ANO-RCC basis sets^{43,44} (copper and donor atoms: ANO-RCC-VTZP; remaining atoms: ANO-RCC-VDZ) were employed in combination with a scalar-relativistic second-order Douglas-Kroll-Hess Hamiltonian and the Cholesky decomposition of the two-electron integrals with a threshold of 10^{-8} . Subsequently, SO-RASSI calculations were carried out to take spin-orbit coupling into account. Magnetic parameters like single-ion *g* factors were obtained from the CASSCF/RASSI-SO wavefunction using the SINGLE_ANISO program from OpenMolcas. For **A'** and **B** electric-field-dependent DFT (EFD-DFT) geometry optimizations were performed along the polar crystallographic *c* axis. These EFD-DFT-optimized structures have been subsequently used in CASSCF/RASSI-SO calculations to study the ionic effect (δg^{disp}) in Cu_3 (see Supplementary Note 8 for further details).

Simulations

The simulations of the EPR and EFM-EPR spectra were realized with EasySpin v6.0.0³⁴, a computational package for spectral simulation and analysis in EPR. As a first step, to simulate solid state CW EPR spectra, the SH of the system is supplied to the program, together with the orientations of the tensors with respect to the molecular frame, which is related to the laboratory frame. Each investigated orientation is then specified with respect to the laboratory frame. The magnetic field is also fixed in the laboratory frame, as well as the \mathbf{B}_1 field of microwave radiation. The program calculates the field-dependent energies of the spin states by finding the eigenvalues of the SH corresponding to the specified orientation, and subsequently the

resonance positions and transition probabilities. Finally, from these values the absorption spectrum is reconstructed. Eventually, through appropriate convolution functions, the final spectrum is shown as the desired harmonic.

The EFM-EPR spectra were simulated as the difference between the absorption (A) spectrum corresponding to $+\mathbf{E}_m$ and that corresponding to $-\mathbf{E}_m$. Indeed, the effect of the electric field modulation in combination with phase-sensitive detection in first harmonic is like a magnetic field modulation in that the first derivative of the absorption signal vs. \mathbf{E}_m is sensed. In this frame, since the variations induced by the applied electric field are small, $A(+\mathbf{E}_m) - A(-\mathbf{E}_m)$ is proportional to the first derivative of A with respect to \mathbf{E}_m ^{23,45}, thus justifying the simulation approach followed for the EFM-EPR. Hyperfine coupling was not explicitly included in the simulations unless otherwise stated, and its effect on the broadening of the lines along z was accounted for using a H_{strain} parameter. For further details, see Supplementary Notes 3 and 9.

Data availability

Source data and optimized structures under electric fields are provided with this paper.

References

- Spaldin, N. A. & Fiebig, M. The renaissance of magnetoelectric multiferroics. *Science* **309**, 391–392 (2005).
- Khomskii, D. Classifying multiferroics: Mechanisms and effects. *Physics* **2**, 20 (2009).
- Matsukura, F., Tokura, Y. & Ohno, H. Control of magnetism by electric fields. *Nat. Nanotechnol.* **10**, 209–220 (2015).
- Fiebig, M., Lottermoser, T., Meier, D. & Trassin, M. The evolution of multiferroics. *Nat. Rev. Mater.* **1**, 16046 (2016).
- Multiferroics march on. *Nat. Mater.* **18**, 187 (2019).
- Spaldin, N. A. & Ramesh, R. Advances in magnetoelectric multiferroics. *Nat. Mater.* **18**, 203–212 (2019).
- Van Slageren, J. Spin–electric coupling. *Nat. Mater.* **18**, 300–301 (2019).
- Golovach, V. N., Borhani, M. & Loss, D. Electric-dipole-induced spin resonance in quantum dots. *Phys. Rev. B* **74**, 165319 (2006).
- Liu, Z. et al. Electric field manipulation enhanced by strong spin-orbit coupling: promoting rare-earth ions as qubits. *Natl. Sci. Rev.* **7**, 1557–1563 (2020).
- Liu, J. et al. Quantum coherent spin–electric control in a molecular nanomagnet at clock transitions. *Nat. Phys.* **17**, 1205–1209 (2021).
- Kane, B. E. A silicon-based nuclear spin quantum computer. *Nature* **393**, 133–137 (1998).
- Trif, M., Troiani, F., Stepanenko, D. & Loss, D. Spin-electric coupling in molecular magnets. *Phys. Rev. Lett.* **101**, 217201 (2008).
- Trif, M., Troiani, F., Stepanenko, D. & Loss, D. Spin electric effects in molecular antiferromagnets. *Phys. Rev. B* **82**, 045429 (2010).
- Islam, M. F., Nossa, J. F., Canali, C. M. & Pederson, M. First-principles study of spin-electric coupling in a {Cu3} single molecular magnet. *Phys. Rev. B* **82**, 155446 (2010).
- Bulaevskii, L. N., Batista, C. D., Mostovoy, M. V. & Khomskii, D. I. Electronic orbital currents and polarization in Mott insulators. *Phys. Rev. B* **78**, 024402 (2008).
- Khomskii, D. I. Spin chirality and nontrivial charge dynamics in frustrated Mott insulators: Spontaneous currents and charge redistribution. *J. Phys. Cond. Matter* **22**, 164209 (2010).
- Khomskii, D. I. Electric dipoles on magnetic monopoles in spin ice. *Nat. Commun.* **3**, 904 (2012).
- Islam, M. F., Withanage, K. P. K., Canali, C. M. & Pederson, M. R. Noncollinear first-principles studies of the spin-electric coupling in frustrated triangular molecular magnets. *Phys. Rev. B* **109**, 214407 (2024).
- le Mardel , F. et al. Probing spin-electric transitions in a molecular exchange qubit. *Nat. Commun.* **16**, 1198 (2025).
- Nossa, J. F., Islam, M. F., Canali, C. M. & Pederson, M. R. First-principles studies of spin-orbit and Dzyaloshinskii-Moriya interactions in the {Cu 3} single-molecule magnet. *Phys. Rev. B* **85**, 085427 (2012).
- Ferrer, S. et al. Antisymmetric exchange in triangular tricopper(II) complexes: Correlation among structural, magnetic, and electron paramagnetic resonance parameters. *Inorg. Chem.* **51**, 985–1001 (2012).
- Choi, K. Y. et al. Observation of a half step magnetization in the {Cu3}-type triangular spin ring. *Phys. Rev. Lett.* **96**, 107202 (2006).
- Mims, W. B. *The Linear Electric Field Effect in Paramagnetic Resonance*. (Oxford University Press, USA, 1976).
- Liu, J. et al. Electric Field Control of Spins in Molecular Magnets. *Phys. Rev. Lett.* **122**, 37202 (2019).
- Boudalis, A. K., Robert, J. & Turek, P. First Demonstration of Magnetoelectric Coupling in a Polynuclear Molecular Nanomagnet: Single-Crystal EPR Studies of $[\text{Fe}_3\text{O}(\text{O}_2\text{CPh})_6(\text{py})_3]\text{ClO}_4 \cdot \text{py}$ under Static Electric Fields. *Chem. Eur. J.* **24**, 14896–14900 (2018).
- Robert, J., Parel, N., Turek, P. & Boudalis, A. K. Polyanisotropic magnetoelectric coupling in an electrically controlled molecular spin qubit. *J. Am. Chem. Soc.* **141**, 19765–19775 (2020).
- Lewkowitz, M. et al. Direct observation of electric field-induced magnetism in a molecular magnet. *Sci. Rep.* **13**, 2769 (2023).
- Wysling, P. & Muller, K. A. Electric-field-modulated resonance lines of non-Kramers ions. *J. Phys. C: Solid State Phys.* **9**, 635–645 (1975).
- Maisuradze, A., Shengelaya, A., Berger, H., Djoki, D. M. & Keller, H. Magnetoelectric coupling in single crystal Cu_2OSeO_3 studied by a novel electron spin resonance technique. *Phys. Rev. Lett.* **108**, 247211 (2012).
- Fittipaldi, M. et al. Electric field modulation of magnetic exchange in molecular helices. *Nat. Mater.* **18**, 329–334 (2019).
- Kintzel, B. et al. Spin–Electric Coupling in a Cobalt(II)-Based Spin Triangle Revealed by Electric-Field-Modulated Electron Spin Resonance Spectroscopy. *Angew. Chem. Int. Ed.* **60**, 8832–8838 (2021).
- Kintzel, B. et al. Molecular electronic spin qubits from a spin-frustrated trinuclear copper complex. *Chem. Commun.* **54**, 12934–12937 (2018).
- Spielberg, E. T. et al. A spin-frustrated trinuclear copper complex based on triaminoguanidine with an energetically well-separated degenerate ground state. *Inorg. Chem.* **54**, 3432–3438 (2015).
- Stoll, S. & Schweiger, A. EasySpin, a comprehensive software package for spectral simulation and analysis in EPR. *J. Magn. Reson.* **178**, 42–55 (2006).
- Bates, C. A. The linear electric field effect on the electron paramagnetic resonance spectrum of Cu^{2+} ions in tetrahedral crystal fields. *J. Phys. C: Solid State Phys.* **1**, 877–888 (1968).
- Bates, C. A. Electric field effects in electron paramagnetic resonance spectra of Cu^{2+} -doped crystals. *J. Phys. C: Solid State Phys.* **2**, 476–483 (1969).
- Solomon, E. I. & Lever, A. B. P. *Inorganic Electronic Structure and Spectroscopy. Volume I*. (Wiley-Interscience, New York, 1999).
- Peisach, J. & Blumberg, W. E. Structural Implications Derived from the Analysis of Electron Paramagnetic Resonance Spectra of Natural and Artificial Copper Proteins. *Arch. Biochem. Biophys.* **165**, 691–708 (1974).
- TURBOMOLE V7.2 2017, a development of University of Karlsruhe and Forschungszentrum Karlsruhe GmbH, 1989–2007, TURBOMOLE GmbH, since 2007; available from <http://www.turbomole.com>
- Weigend, F. & Ahlrichs, R. Balanced basis sets of split valence, triple zeta valence and quadruple zeta valence quality for H to Rn: Design and assessment of accuracy. *Phys. Chem. Chem. Phys.* **7**, 3297–3305 (2005).

41. Reed, A. E., Weinstock, R. B. & Weinhold, F. Natural population analysis. *J. Chem. Phys.* **83**, 735–746 (1985).
42. Fdez. Galván, I. et al. OpenMolcas: From Source Code to Insight. *J. Chem. Theory Comput* **15**, 5925–5964 (2019).
43. Roos, B. O., Lindh, R., Malmqvist, P. Å, Veryazov, V. & Widmark, P. O. Main Group Atoms and Dimers Studied with a New Relativistic ANO Basis Set. *J. Phys. Chem. A* **108**, 2851–2858 (2004).
44. Roos, B. O., Lindh, R., Malmqvist, P. Å, Veryazov, V. & Widmark, P. O. New relativistic ANO basis sets for transition metal atoms. *J. Phys. Chem. A* **109**, 6575–6579 (2005).
45. Poole, C. P. *Electron Spin Resonance: A Comprehensive Treatise on Experimental Techniques*. (New York: Interscience, 1967).

Acknowledgements

M.F. is grateful to Giampaolo Tobia and Antonio Orlando for technical assistance. Stefan Stoll is gratefully acknowledged for his assistance with EasySpin, and Lorenzo Tesi is thanked for his aid in crystal mounting. B.K. gratefully acknowledges COST Action 15128 on Molecular Spintronics (MOLSPIN) for enabling a short-term scientific mission to Florence. The support of the Italian MUR through the FIS project ELECOS (FIS00001045) (RS) and Dipartimenti di Eccellenza 2023-2027 (DICUS 2.0) (R.S. and M.P.) is acknowledged. Funding by the European Union through ERC-StG ELECTRA, 101039890 (M.P.) and FET FATMOLS, GA862893 (R.S.) is acknowledged. Views and opinions expressed are however those of the author(s) only and do not necessarily reflect those of the European Union or the European Research Council. Neither the European Union nor the granting authority can be held responsible for them. The financial support provided by INFN through the project NAMASSTE (M.F.) is acknowledged. The position of A.C. was financed through the project NAMASSTE-UNIFI funded by Banca d'Italia. Funding by the Deutsche Forschungsgemeinschaft (DFG, German Research Foundation) for project number 549658201 is acknowledged (W.P.).

Author contributions

M.F., W.P. and R.S. conceived the research. B.K. synthesized the materials and grew the crystals. A.C., B.K., M.F. and M.P. recorded the spectra. M.P. cured crystallographic analysis and crystal orientation. M.B. developed computational models and performed ab initio calculations. A.C., M.B. and M.F. simulated the EPR and EFM-EPR spectra. All authors have critically followed each aspect of the research and contributed to drafting and editing the manuscript.

Competing interests

The authors declare no competing interests.

Additional information

Supplementary information The online version contains supplementary material available at <https://doi.org/10.1038/s41467-025-61417-6>.

Correspondence and requests for materials should be addressed to Winfried Plass, Roberta Sessoli or Maria Fittipaldi.

Peer review information *Nature Communications* thanks Carlo Canali, and the other, anonymous, reviewer(s) for their contribution to the peer review of this work. A peer review file is available.

Reprints and permissions information is available at <http://www.nature.com/reprints>

Publisher's note Springer Nature remains neutral with regard to jurisdictional claims in published maps and institutional affiliations.

Open Access This article is licensed under a Creative Commons Attribution-NonCommercial-NoDerivatives 4.0 International License, which permits any non-commercial use, sharing, distribution and reproduction in any medium or format, as long as you give appropriate credit to the original author(s) and the source, provide a link to the Creative Commons licence, and indicate if you modified the licensed material. You do not have permission under this licence to share adapted material derived from this article or parts of it. The images or other third party material in this article are included in the article's Creative Commons licence, unless indicated otherwise in a credit line to the material. If material is not included in the article's Creative Commons licence and your intended use is not permitted by statutory regulation or exceeds the permitted use, you will need to obtain permission directly from the copyright holder. To view a copy of this licence, visit <http://creativecommons.org/licenses/by-nc-nd/4.0/>.

© The Author(s) 2025